

Interfacial Properties of Monolayer and Bilayer MoS₂ Contacts with Metals: Depressed Many-electron Effects

Hongxia Zhong,¹ Zeyuan Ni,¹ Yangyang Wang,¹ Meng Ye,¹ Zhigang Song,¹ Yuanyuan Pan,¹ Ruge Quhe,^{1,4} Jinbo Yang,^{1,2} Li Yang,³ Junjie Shi,^{1,*} and Jing Lu^{1,2,*}

¹State Key Laboratory for Mesoscopic Physics and Department of Physics, Peking University, Beijing 100871, P. R. China

²Collaborative Innovation Center of Quantum Matter, Beijing 100871, P. R. China

³Department of Physics, Washington University in St. Louis, St. Louis, Missouri 63130, USA

⁴Academy for Advanced Interdisciplinary Studies, Peking University, Beijing 100871, P. R. China

Email: jjshi@pku.edu.cn; jinglu@pku.edu.cn

ABSTRACT

Although many devices based on MoS₂ have been fabricated, where MoS₂-metal contact plays a critical role, the nature of MoS₂-metal contact has not been well established yet. We provide the first comparative study of the interfacial properties of a series of monolayer (ML) and bilayer (BL) MoS₂-metal contacts (metal = Sc, Ti, Ag, Pt, Ni, and Au) with inclusion of many-electron effects based on a dual interface model. A comparison between the calculated and observed Schottky barrier heights (SBHs) suggests that many-electron effects are strongly depressed and become ineligible when channel MoS₂ is doped by electrodes. Ohmic contact is revealed for both ML and BL MoS₂-Sc contacts, and Schottky barrier prevails in other contacts, with the SBH decreased by the interlayer coupling. The dual interface model with suppression of the many-electron effects can be expanded to a general device with metal-semiconductor interface.

Subject Areas: Computational Physics, Electronics, Nanophysics

I. INTRODUCTION

Owing to their excellent properties, two-dimensional (2D) molybdenum disulfide MoS_2 has attracted much recent attention [1-6]. A variety of devices based on 2D MoS_2 have been fabricated, such as field-effect transistors (FETs) [7-9], inverters [10], fully integrated circuits [11], sensors [12], photoelectronic devices [13], phototransistors [14,15], spintronic devices [16], and valleytronic devices [17,18]. Among 2D MoS_2 , monolayer (ML) and bilayer (BL) MoS_2 attract the most attention [2,3,5,6-18]. They show quite interesting differences and make up a pair of complementary materials: (1) ML MoS_2 has a larger direct band gap, while BL MoS_2 possesses a smaller indirect band gap. Correspondingly, photoluminescence is dramatically enhanced in ML MoS_2 [6,19]. (2) ML MoS_2 is inversion asymmetric and serves as an ideal quantum valley Hall insulator (QVHI) [1]. By contrast, inversion symmetric BL MoS_2 is not a QVHI, but it can be transformed into a QVHI with a tunable valley magnetic moment by a vertical electric field [5]. (3) Zeeman-like spin splitting is intact by a vertical electric field in ML MoS_2 but it becomes tunable in BL MoS_2 [16].

In a real device, semiconducting 2D MoS_2 needs a contact with metal electrodes, and the formation of low-resistance metal contacts is the biggest challenge that masks the intrinsic exceptional electronic properties of 2D MoS_2 , and many efforts have been made to study 2D MoS_2 -metal contact so as to reduce the Schottky barrier height (SBH) [20-22]. The experiments found that the SBH and transport properties of 2D MoS_2 -metal contact strongly depend on not only the work function of metal but also the MoS_2 layer number. For example, there is a significant SBH between Ti and ML MoS_2 [23,24]; by contrast, Ti forms an Ohmic contact with BL MoS_2 at room temperature and a Schottky contact with a small SBH of ~ 0.065 eV at a low temperature [11,25]. The microscopic physical picture of 2D MoS_2 -metal interfaces is highly desirable, which not only provides an insight into the observed phenomenon in 2D MoS_2 -metal interfaces but also helps to optimize 2D MoS_2 devices by reducing SBH. There are several theoretical attempts to establish a microscopic physical picture of ML MoS_2 -metal interfaces [21,22,24,26,27], however, to the best of our knowledge, a clear and comprehensive microscopic physical picture on BL MoS_2 -metal interfaces is still lacking at present.

To establish a correct microscopic physical picture on BL MoS_2 -metal interfaces. Two

things have to be taken into accounts carefully. First, there are two possible interfaces to form Schottky barrier in a MoS₂ transistor [22,28]: one is the source/drain interface (B) between the contacted MoS₂ and the metal surface in the vertical direction (see Fig. 7(b)), and the other is source/drain-channel (D) interface between the contacted MoS₂ and channel MoS₂ in the lateral direction (see Fig. 7(b)). However, most of the previous theoretical studies of ML MoS₂-metal interfaces except the works of Banerjee *et al.* [22,28] only consider the vertical interface, ignoring the lateral one. For example, Igor *et al.* [21] predicted that Ti forms a low-resistance Ohmic contact to ML MoS₂ inferred from the gap states from the vertical interface calculation, which is in contrast to the significant SBH experimentally [23]. To interpret the experimental observations, we should employ an improved dual interface model that distinguishes the two types of Schottky interfaces in a transistor device. However, it is unclear whether Ohmic contact remains available for ML MoS₂-metal in terms of the dual interface model.

Secondly, because the SBH at the metal-semiconductor interfaces depends on the difference between the Fermi level (E_f) of the metal and the band edge positions of the semiconductor, the band edge positions of the semiconductor must be accurately determined [29,30]. It is well known that the Kohn–Sham density functional theory (KS-DFT) fails to do so because it is a single-electron theory. A feasible method to determine the accurate band edge positions of a free-standing semiconductor is first-principles many-electron Green function approach within the GW approximation, where electron-electron correlation effects are treated properly [13,31-35]. The DFT and GW band gaps are 1.86 (1.30) and 2.84 (1.82) eV for ML (BL) MoS₂ [36,37], respectively. In a real device, for the semiconductor fully under metal (namely, in the electrode region), the many-electron effects, however, are greatly depressed if a charge transfer takes place [38,39]; as a result, the KS band edge positions and band gap are a good approximation. However, for the semiconductor in the channel, it is unknown whether the many-electron effects should be included to generate the correct band structure. Any direct GW calculation to solve this issue is difficult limited by the computational resource. Consequently, it is unclear whether the many-electron effects should be considered in calculating the lateral SBH of a device. In other word, it is unclear whether the transport gap of a MoS₂ device is equal to the DFT band gap or quasiparticle band gap of

freestanding MoS₂.

In this Article, we provide a comparative study of the interfacial properties of ML and BL MoS₂ on several commonly used metals (Sc, Ti, Ag, Pt, Ni, and Au) [8,20], for the first time by using DFT method with inclusion of the *GW* correction to the band edge positions and the dual interface model. The excellent agreement between the observed and calculated SBH in BL MoS₂-Ti interface at the DFT level provides an indirect evidence that *GW* correction to the band edge positions is unnecessary if the Fermi level of the electrodes is not in line with the band gap center of the channel. Such a depression of many-electron effects can be applied to a general metal-semiconductor interface.

II. METHODOLOGY

We use six layers of metal atoms (Ni, Ag, Pt, and Au in (111) orientation and Sc and Ti in (0001) orientation) to model the metal surface and construct a supercell with ML and BL MoS₂ adsorbed on one side of the metal surface. BL MoS₂ takes AB stacking mode (with a D_{3d} point group symmetry) in our model. The calculated in-plane lattice constant $a = 3.166 \text{ \AA}$, which is in good agreement with the experimental value 3.160 \AA [40]. The MoS₂ 1×1 unit cell is adjusted to the 1×1 unit cells of Sc and Ti(0001) faces, and the MoS₂ $\sqrt{3} \times \sqrt{3}$ unit cell is adjusted to 2×2 unit cells [26]. The lattice constant mismatches with respect to that of MoS₂ are $1.2 \sim 9.1\%$. A vacuum buffer space of at least 15 \AA is set to ensure decoupling between neighboring slabs. MoS₂ mainly interacts with the topmost three layers metal atoms [21], so cell shape and the bottom three layers of metal atoms are fixed.

The geometry optimization and electronic properties of periodic structures are performed using the projector augmented wave (PAW) method implemented in the Vienna *ab initio* simulation package (VASP) code [41,42]. The generalized gradient approximation (GGA) functional to the exchange-correction functional, of the Perdew–Wang 91 (PW91) form [43] with vdW corrections [44], and the PAW pseudopotential are adopted [42]. The cut off energy is set to 500 eV after convergence tests. An equivalent Monkhorst-Pack k -points grid [45] of $25 \times 25 \times 1$ for a MoS₂ unit cell is chosen for supercell relaxations and $30 \times 30 \times 1$ for property calculations. Dipole corrections in the z direction are used in all calculations.

III. RESULTS AND DISCUSSION

A. Geometry and stability of ML and BL MoS₂-metal interfaces

After optimizing the structures from 6 initial configurations in an interface with 1×1 MoS₂ unit cell and 3 initial configurations in an interface with $\sqrt{3} \times \sqrt{3}$ MoS₂ unit cell, we obtain the most stable configurations of the ML MoS₂-metal interfaces, as shown in Fig. 1. The initial configurations of BL MoS₂-metal interfaces are constructed on the basis of the most stable ML MoS₂-metal interfaces. On Sc(0001), the Mo atoms in the primitive cell sit above the top metal atom, and the S atoms sit above the second layer metal atom; While on Ti(0001), the Mo atoms in the primitive cell still sit above the top metal atom, but the S atoms sit above the centers of triangles. On Ni and Pt(111), the three Mo atoms in the supercell sit above the fcc hollow, hcp hollow, and top sites, respectively. In the cases of Ag and Au(111), the Mo atoms are all above the centers of the triangles formed by the fcc, hcp, and top sites. The calculated key parameters of ML and BL MoS₂-metal interfaces studied in this work are summarized in Table 1. When ML and BL MoS₂ are in contact with metals, the equilibrium distances d_{S-M} range from 1.557 ~ 3.405 Å, increasing in the order of Ti < Sc < Ni < Pt < Ag < Au. The binding energies E_b have a reversal order, i.e., Ti > Sc > Ni > Pt > Ag > Au, since a smaller d_{S-M} generally causes a larger binding energy. ML and BL MoS₂-metal contacts nearly share the same d_{S-M} and E_b . The binding of MoS₂ to metal surfaces ($E_b = 0.307 \sim 1.848$ eV per surface sulfur atom [21,26]) is considerably stronger than that of graphene to metal surfaces, with the binding energy of 0.027 ~ 0.327 eV per carbon atom [46]. Such a difference is reasonable because MoS₂ is chemically more reactive than graphene. We note that previous DFT calculations indicate that the E_b of ML MoS₂ on Ir, Pd, and Ru surfaces ranges from 0.62 ~ 0.82 eV per surface sulfur atom [26]. Similar to the case of graphene [46], the adsorption of ML and BL MoS₂-metal surfaces can be classified into either chemisorption (Sc, Ti, Ni, and Pt) or physisorption (Ag and Au) in terms of the E_b and d_{S-M} . Sc, Ti, Ni, and Pt have open d shells and interact with MoS₂ strongly, whereas s -electron metals Ag and Au have closed d shells and interact with MoS₂ weakly.

B. Electronic structure of ML and BL MoS₂-metal interfaces

The electronic structures of free-standing ML MoS₂ and the interfacial systems are presented in Fig. 2. Free-standing ML MoS₂ has a direct band gap of 1.68 eV, consistent with

the reported PBE value of 1.67 eV [47]. The band structures of ML MoS₂-metal contacts are classified into three categories in terms of the hybridization degree of ML MoS₂ on metals. The band structure of ML MoS₂ is identifiable clearly for MoS₂ on Au surface, as a result of weak charge-transfer interaction and dispersion interaction between ML MoS₂ and Au surface. The band structure of ML MoS₂ is destroyed seriously by Sc, Ti, and Ni surfaces and slightly destroyed by Pt and Ag surfaces, because the outmost electrons of the five metals except Ag are *d* electrons, which strongly hybridize with the states near the Fermi level E_f of ML MoS₂. The electronic structures of free-standing BL MoS₂ and BL MoS₂-metal interfaces are shown in Fig. 3, with a smaller indirect band gap of 1.46 eV for free-standing BL MoS₂. The band hybridization degree is similar from ML to BL MoS₂ and can be also divisible into the same three categories.

In order to have a deep understanding for the hybridization in Figs. 2 and 3, we further calculate the partial density of states (PDOS) on Mo and S orbitals for ML and BL MoS₂-metal contacts as shown in Figs. 4 and 5. Upon making a contact with Sc, Ti, Ni, Pt, and Ag, the MoS₂-metal interface becomes metallic since there are electronic states in the original band gap of MoS₂. Among the five contact metals, Sc and Ti modify the electronic states near E_f much more than others. The MoS₂-Sc (Ti) contact possesses a broadening peak, obvious dispersive bands, and delocalized states near E_f at the interface. In the MoS₂-Sc system, the contribution of S 3*sp* and Mo 4*d_{xy}* states dominate E_f , which is associated with a strong S-Sc mixing. E_f is dominated by Mo 4*d_{xy}* states, with the other states playing a minor role in the MoS₂-Ti system. There is no state in the original MoS₂ band gap in MoS₂-Au system, indicating that MoS₂ preserves the semiconducting nature on Au surface.

Large charge carrier density at the source/drain interface B indicates a strong overlap of electron orbitals and sufficient injection of electron into the MoS₂ layer [21]. The electron densities averaged in planes parallel to the interface ρ_l of the investigated six ML MoS₂-metal contacts are displayed in Fig. 6. We can see from Fig. 6 that ρ_l at the chemisorption interfaces (Sc, Ti, Ni, and Pt) is higher than that at the physisorption interfaces (Ag and Au), a difference compared with the PDOS analysis in Fig. 4. This difference implies that the chemisorption interface have a larger possibility to achieve a lower contact resistance.

C. Many-electron effects

The accurate SBH at a metal-semiconductor interface depends on the absolute band-edge positions of the semiconductor. Because the DFT method seriously underestimates the band gap of a semiconductor, the inclusion of the GW correction is also necessary to obtain a correct band gap and absolute band-edge positions of a freestanding (or undoped) semiconductor. If the band gap center (BGC) or Fermi level E_f or work function and the GW corrected band gap (E_g^{GW}) of the semiconductor are available, the absolute energies at the conduction band maximum (CBM) and the valence band minimum (VBM) can be obtained via the relation:

$$E_{CBM}^{GW} = E_f + \frac{1}{2} E_g^{GW} \quad (1)$$

$$E_{VBM}^{GW} = E_f - \frac{1}{2} E_g^{GW} \quad (2)$$

Unfortunately, in many cases, the BGC of a semiconductor is unavailable. A common solution [29,30] is to assume that the BGC at the DFT level is unchanged after the GW correction (named GW -BGC approximation). Fig. 7(a) illustrates the GW correction to the absolute band positions in BGC approximation. Based on the GW -BGC scheme, the calculated ionization potential (IP = 5.45 eV) and electron affinity (χ = 4.22 eV) of bulk MoS₂, compared with values of 5.33 and 4.45 eV at the DFT level [29], are in good agreement with the experimental values (IP = 5.47 ± 0.15 eV and χ = 4.07 ± 0.35 eV) [48]. Actually, Yang *et al.* [49] found that the absolute band-edge energies for ML dichalcogenides given by the direct GW method and the GW -BGC scheme are quite similar. Therefore, the GW -BGC approximation is a good approximation for our studied MoS₂ systems.

The GW corrections to the band gap of free-standing ML ($E_g^{GW} = 2.84$ eV) and BL ($E_g^{GW} = 1.82$ eV) MoS₂ are available [36,37]. In our calculations for the SBH at the vertical direction, we take the GW -BGC approximation to determine the absolute band edge positions. In our calculations for the SBH at the lateral direction, we determine the GW -corrected absolute band position by taking the experimental work function (5.25 eV [50]) of free-standing BL MoS₂ (namely channel BL MoS₂) as the BGC and further assume free-standing ML and BL MoS₂ share identical BGC. The calculated work function of free-standing BL MoS₂ at the DFT level is 5.04 eV, which is 0.21 eV slightly smaller than its experimental value. The

calculated work function of free-standing ML MoS₂ at the DFT level is merely 0.08 eV greater than the calculated one of free-standing BL MoS₂.

D. Schottky barrier at ML MoS₂-metal interfaces

The band structures of ML MoS₂ on the metal surfaces are shown in Fig. 2. A band hybridization has taken place for MoS₂ on Sc, Ti, Ni, Pt, and Ag surfaces, resulting in absence of vertical Schottky barrier for the five contacts. By contrast, the band structure of ML MoS₂ is identifiable, and E_f is nearly in the middle of the band gap. As a result, there is a quite large vertical n -type (or p -type) Schottky barrier in terms of the difference between E_f of the interfacial system and the CBM (or VBM) of ML MoS₂, with $\phi_v^{DFT} = 0.763$ eV and $\phi_v^{GW} = 1.343$ eV for MoS₂ contacted Au electrodes. The obviously smaller SBHs from the DFT method than that with the GW correction is attributed to the fact that the band gap (1.68 eV) of ML MoS₂ calculated by the DFT method is much smaller than that (2.84 eV) by the GW method [36]. Many-electron effects are probably important in ML MoS₂-Au contact because the doping level of ML MoS₂ by Au is rather small.

Lateral Schottky barrier Φ_L is formed at the interface D (see Fig. 7(b)) and determined by the energy difference between E_f of the interfacial system and the CBM (n -type) or VBM (p -type) of channel ML MoS₂. ML MoS₂ forms an Ohmic contact with Sc in the lateral direction at the DFT level since E_f of the interfacial system is higher than the E_{CBM}^{DFT} of channel MoS₂. However, there is a large lateral SBH at the GW level, with $\phi_L^{GW} = 0.539$ eV. There is a lateral Schottky barrier for Ti, Ag, Pt, and Ni contacts at both the DFT and GW levels, with smaller $\phi_L^{DFT} = 0.187$ (Ti), 0.252 (Ag), 0.546 (Pt), 0.591 (Ni) eV and larger $\phi_L^{GW} = 0.731$ (Ti), 0.832 (Ag), 1.226 (Pt), 1.171 (Ni) eV. When ML MoS₂ is in contact with Au electrodes, the contacted and channel MoS₂ have nearly the same absolute E_f , leading to zero Φ_L for MoS₂-Au at both levels.

The DFT SBHs of ML MoS₂-metal interfaces are in good agreement with the previous DFT calculations (see Table 1). For example, the Φ_v and Φ_L for ML MoS₂-Au interface are calculated to be 0.763 and 0.000 eV, respectively. These two values are in good agreement with other DFT values of 0.88 and 0.000 eV [27], respectively. In the previous theoretical work, it is claimed that Ti forms a low-resistance Ohmic contact to ML MoS₂ based on $\Phi_v =$

0.00 [21]. This is apparently inconsistent with the experiment where a significant SBH at the ML MoS₂-Ti junction has been observed [23]. The dual interface model, however, gives a lateral SBH of 0.187 eV at the DFT level for ML MoS₂-Ti interface, which is in qualitative agreement with the experiment [23] and other DFT value of 0.33 eV [22]. Therefore, the inclusion of the lateral Schottky barrier in terms of the dual interface model is necessary to predict a right metal-semiconductor contact nature.

E. Schottky barrier at BL MoS₂-metal interfaces

The band structures of BL MoS₂ on the metal surfaces are shown in Fig. 3. The vertical Ohmic contact feature remains on Sc, Ti, Ni, Pt, and Ag surfaces from ML to BL MoS₂, because the band hybridization remains. From ML to BL MoS₂, Φ_V in MoS₂-Au contact is significantly decreased by 0.096 and 0.510 eV at the DFT and *GW*-BGC schemes, respectively, as a result of the reduction of the band gap (0.220 eV at the DFT level and 1.020 eV at the *GW* level). BL MoS₂ forms an Ohmic contact with Sc and Au in the lateral direction. Therefore, Sc also forms an Ohmic contact to BL MoS₂, as the case of ML MoS₂-Sc contact, with neither vertical nor lateral Schottky barrier. The Ohmic contact means high electron injection efficiency, which is highly eager for MoS₂-based devices. The lateral SBHs for Ag, Pt, and Ni contacts are significantly decreased by 0.409, 0.542, and 0.409 eV, respectively, at the *GW* level, and slightly decreased by 0.009, 0.042, and 0.009 eV, respectively, at the DFT level from ML to BL MoS₂. The reduced SBH from ML to BL MoS₂ is in good agreement with the experiment [20].

The BL MoS₂-Ti is a Schottky contact with a Φ_L^{DFT} of 0.096 eV at the DFT level, which is quantitative consistent with the experimental value ~ 0.065 eV extracted by low-temperature measurement [25]. By contrast, the SBH is as high as 0.276 eV at the *GW* level. The apparently better agreement between Φ_L^{DFT} and the measured Φ_L compared with Φ_L^{GW} suggests that many-electron effects have been greatly depressed by the charge transfer between channel MoS₂ and the electrodes, which significantly screens electron-electron Coulomb interaction and validates sing-electron approximation. In other word, the transport gap of MoS₂ is determined by the DFT band gap rather than the quasiparticle band gap.

In our above calculations, we adapt the lattice constant of MoS₂ to that of metal surfaces as

the match way in Ref. [26] in view of the fact that the bulk metal electrode is more robust than ML and BL MoS₂. We note that the lattice constant of MoS₂ is fixed in Ref. [27]. In order to explore the effects of the match way on the work function of MoS₂-metal interface, we give the work function of interfacial systems in the case of fixing MoS₂ lattices in Table 2. The work function of the system with Ti surface adjusted to MoS₂ is 0.205 eV smaller than that of the system with BL MoS₂ adjusted to Ti surface; consequently, the lateral SBH disappears. Such a result is inconsistent with the experimental SBH of 0.065 eV for BL MoS₂-Ti contact. There are nearly no difference in work function between these two strained method for BL MoS₂-Sc and ML MoS₂-Ti contacts.

Since the lattice mismatches are large for the Sc-MoS₂ (4.485%) and Ti-MoS₂ (6.791%) interfaces in the above study, we further enlarge the supercell to reduce the lattice mismatch. The $\sqrt{13} \times \sqrt{13}$ unit cell of MoS₂ is adjusted to the $2\sqrt{3} \times 2\sqrt{3}$ unit cells of Sc(0001) surface, with the lattice mismatch decreased to 1.29%. The $2\sqrt{3} \times 2\sqrt{3}$ unit cell of MoS₂ is adjusted to $\sqrt{13} \times \sqrt{13}$ unit cells of Ti(0001) surface, with the lattice mismatch decreased to 2.99%. Compared with the large mismatch configuration, the small mismatch ones do not change the contact type and just slightly increase Φ_L^{DFT} from 0.187 (0.096) to 0.216 (0.161) eV for ML (BL) MoS₂-Ti contact, which is in agreement with a DFT value of 0.33 eV of Banerjee *et al.* [28] based on a larger ML MoS₂-Ti interfacial supercell containing 6 Mo and 12 S atoms per unit cell in the contact region. Φ_L^{GW} is increased to 0.341 eV for BL MoS₂-Ti contact, which further deviates from the experimental value of 0.065 eV [25].

In a recent work, the transport gap and SBH of phosphorene have been measured. Phosphorene is *p*-type by Ni electrodes, and the transport gaps of ML and few layer phosphorene with Ni electrodes are in good agreement with the DFT band gaps at the GGA level. For example, the transport gap of ML and BL phosphorene are 0.98 ± 0.4 and 0.71 ± 0.4 eV [51], respectively, and the corresponding band gaps are 0.91 and 0.6 eV at the DFT level [52], while the quasiparticle band gaps are 2.0 and 1.3 eV [53]. The measured *p*-type SBH of ML phosphorene is 0.34 ± 0.2 eV, which is also in good agreement the one at the DFT level (0.28 eV) but much smaller than the one at the *GW* level (0.82 eV) [54]. Therefore, the suppressed many-electron effects can be expanded to a general device if channel

semiconductor is doped by electrodes, and correspondingly the transport gap depends on the DFT band gap instead of the quasiparticle band gap.

F. Tunneling barrier at ML and BL MoS₂-metal interfaces

In order to complete the analysis of contacts, we further investigate the electrostatic potential at the ML MoS₂-metal interfaces and show the results in Fig. 6. The tunneling barrier ΔV here is defined as the potential energy above the Fermi energy between the MoS₂ and metal surfaces, indicated by the black rectangular, and the tunneling width w_B is defined as the full width at half maximum of the ΔV . As shown in Fig. 6 and Table 3, the ΔV values at the chemisorption interfaces (Sc, Ti, Ni, and Pt) are significantly lower and the w_B values are significantly narrower than those at the physisorption ones (Ag and Au). A lower barrier height and a narrower width at a semiconductor-metal interface mean a higher electron injection efficiency. We estimate the tunneling probabilities T_B from metal to MoS₂ using a square potential barrier model as:

$$T_B = \exp\left(-2 \times \frac{\sqrt{2m\Delta V}}{\hbar} \times w_B\right) \quad (3)$$

where m is the effective mass of a free electron and \hbar is the Plank's constant. The T_B values are thus estimated to be 100, 100, 74.33, 53.21, 19.68, and 4.74% for Sc, Ti, Ni, Pt, Ag, and Au contacts, respectively (see Table 3). Apparently, Sc and Ti contacts have perfect transmission. The tunneling properties of the tunneling barrier at the BL MoS₂-metal interfaces are also summarized in Table 3. Compared with the case of ML MoS₂ contact metals, there is little change in the tunneling properties for BL MoS₂, indicating that the tunneling properties are insensitive to the MoS₂ layer number.

In the light of Schottky barrier and tunneling barrier, the nature of MoS₂-metal contact can be classified into five types. Sc can form high quality contact interface with ML and BL MoS₂ with zero tunneling barrier and zero Schottky barrier, leading to Ohmic contact (Figs. 7(c) and 7(h)). Although the metallization of ML MoS₂ with Ti eliminates the Schottky barrier at the interface B, the injected electrons from the metal still confront a n -type Schottky barrier at the interface D, leading to Type 1 in Fig. 7(d). The nature of BL MoS₂-Ti contacts also belong to Type 1. It is worthwhile to note that the tunneling barrier vanishes in Type 1 contact due to the

strong orbital overlaps. Unlike the case in Type 1, there is a tunneling barrier at the interface B in Types 2 and 3 contacts. Only p -type Schottky barrier forms in ML and BL MoS₂-Pt contacts (Type 3, Figs. 7(f) and 7(k)). In Type 4 contact (ML and BL MoS₂-Au), Schottky barrier and tunneling barrier are formed at the interface B, and SBH is zero at the interface D.

G. Fermi level line-up

Our calculated line-up of metal Fermi level with the electronic bands of ML MoS₂ at the DFT level is shown in Fig. 8, in which the GW and direct GW [49] results are also provided for comparison. There is almost no difference between our results and the direct GW results. Compared with pure metal, E_f of the Sc, Ti, Ag, and Pt-ML MoS₂ systems become closer to E_f of ML MoS₂, indicative of existence of a partial Fermi level pinning. The partial Fermi level pinning is a synergic result of the metal work function modification and the interface gap states formation in the studied interface systems [27]. The Fermi levels of Sc, Ti, Ag, Au, and Ni-ML MoS₂ systems are higher than that of the channel ML MoS₂ and form n -type contact, while the Fermi level of Pt-ML MoS₂ absorbed system is lower than that of their channel ML MoS₂ and form p -type contact. The n -type characteristic of ML MoS₂ on Sc, Ti, Ag, Au, and Ni surfaces has been observed experimentally [8,20,23], and the p -type characteristic on Pt surface is calculated in other DFT calculation [27]. Therefore, ML MoS₂ p - n junction can be fabricated by using Sc, Ti, Ag, Au, or Ni to contact one end of ML MoS₂ and Pt to contact the other end of it. The ML MoS₂ p - n junction can be used to develop optoelectronics or valley-optoelectronics technology [55]. Comparing the line-up at the DFT and GW levels, we find that the doping type is unchanged.

The calculated line-up of metal Fermi level with the electronic bands of BL MoS₂ is shown in Fig. 9, in which the GW levels are also listed for reference. Compared with Fig. 8, the GW correction to the band gap of BL MoS₂ is less significant because many-body effect is reduced with the increasing size in the vertical direction. A partial Fermi level pinning to E_f of BL MoS₂ has also been observed since the work functions of the Sc, Ag, and Pt contacted systems (electrode) become closer to E_f of BL MoS₂ compared with pure metal. BL MoS₂ FET is also p -type doped by Pt contact and n -type by the other five contacts. Consistently, the experiments have found n -type characteristic of BL MoS₂ on Ti and Au surfaces [11,25].

The Fermi level shift ΔE_f is defined as the difference between the interfacial systems and

free-standing 2D MoS₂ work functions when the band hybridization occurs at the interfaces (Sc, Ti, Ni, Pt, and Ag contacts). ΔE_f is defined as $\Delta E_f = E_{\text{mid}} - E_f$ for the interface without band hybridization (for Au contact), where E_{mid} is the midpoint of the identifiable band gap of MoS₂. Negative (positive) ΔE_f means *n*-type (*p*-type) doping of 2D MoS₂. The doping types determined from ΔE_f are in agreement with those determined from Figs. 8 and 9. ΔE_f as a function of the difference between the clean metal (W_M) and ML (BL) MoS₂ work functions (W_{MoS_2}) is shown in Fig. 10 (11). The cross point from *n*- to *p*-type doping is $W_M - W_{\text{MoS}_2} = 0.21$ (0.13) eV for ML (BL) case. The ΔE_f has a nearly linear dependence with the $W_M - W_{\text{MoS}_2}$ with a slope of 0.64 in both ML and BL MoS₂-metal contacts, approximately equal to the previously reported theoretical value of 0.71 in ML MoS₂-metal contacts[27]. Notably, ΔE_f is insensitive to the MoS₂ layer number, leading to the same linear relation between ΔE_f and work function. Note that the slope close to 0 indicates a strong Fermi level pinning, and we therefore observe a partial Fermi level pinning picture once more when the six metals contact ML MoS₂.

IV. CONCLUSION

In summary, we provide the first comparative study of the interfacial properties of monolayer and bilayer MoS₂ on Sc, Ti, Ag, Pt, Ni, and Au surfaces by using the DFT method with the inclusion of the *GW* correction to the MoS₂ band edge positions and distinguishing the two types of Schottky interfaces in a 2D MoS₂ transistor device. Many-electron effects remarkably increase the Schottky barrier heights, but the Schottky barrier heights decrease from monolayer to bilayer MoS₂ due to the interlayer coupling. A comparison between the calculated and observed Schottky barrier heights suggests that many-electron effects are strongly depressed and the transport gap of a device depends on the DFT band gap rather than the quasiparticle band gap. No Schottky barrier exists in ML and BL MoS₂-Sc contact, indicating a highest electron injection efficiency from Sc electrode to ML and BL MoS₂. This fundamental study provides a deep insight into 2D MoS₂-metal interfaces, and the chief approach (dual interface model + suppressed many-electron effects) can be expanded to a general metal-semiconductor interface.

ACKNOWLEDGMENT

This work was supported by the National Natural Science Foundation of China (No. 11274016/11364030), the National Basic Research Program of China (No. 2013CB932604/2012CB619304), and the National Science Foundation Grant (1207141).

REFERENCES

- [1] K. F. Mak, K. L. McGill, J. Park, and P. L. McEuen, *Science* **344**, 1489-1492 (2014).
- [2] X. Yin, Z. Ye, D. A. Chenet, Y. Ye, K. O'Brien, J. C. Hone, and X. Zhang, *Science* **344**, 488-490 (2014).
- [3] J. Stajic, *Science* **344**, 1476-1478 (2014).
- [4] C.-H. Lee, G.-H. Lee, A. M. Zande, W. Chen, Y. Li, M. Han, X. Cui, G. Arefe, C. Nuckolls, T. F. Heinz, J. Guo, J. Hone, and P. Kim, *Nature Nanotech.* **150**, 676-681 (2014).
- [5] S. Wu, J. S. Ross, G.-B. Liu, G. Aivazian, A. Jones, Z. Fei, W. Zhu, D. Xiao, W. Yao, D. Cobden, and X. Xu, *Nature Phys.* **9**, 149-153 (2013).
- [6] K. F. Mak, C. Lee, J. Hone, J. Shan, and T. F. Heinz, *Phys. Rev. Lett.* **105**, 136805 (2010).
- [7] B. W. H. Baugher, H. O. H. Churchill, Y. Yang, and P. Jarillo-Herrero, *Nano Lett.* **13**, 4212-4216 (2013).
- [8] B. Radisavljevic, A. Radenovic, J. Brivio, V. Giacometti, and A. Kis, *Nature Nanotech.* **6**, 147-150 (2011).
- [9] D. Sarkar, W. Liu, X. Xie, A. C. Anselmo, S. Mitragotri, and K. Banerjee, *ACS Nano* **8**, 3992-4003 (2014).
- [10] B. Radisavljevic, M. B. Whitwick, and A. Kis, *ACS Nano* **5**, 9934-9938 (2011).
- [11] H. Wang, L. Yu, Y.-H. Lee, Y. Shi, A. Hsu, M. L. Chin, L.-J. Li, M. Dubey, J. Kong, and T. Palacios, *Nano Lett.* **12**, 4674-4680 (2012).
- [12] F. K. Perkins, A. L. Friedman, E. Cobas, P. M. Campbell, G. G. Jernigan, and B. T. Jonker, *Nano Lett.* **13**, 668-673 (2013).
- [13] R. S. Sundaram, M. Engel, A. Lombardo, R. Krupke, A. C. Ferrari, P. Avouris, and M. Steiner, *Nano Lett.* **13**, 1416-1421 (2013).
- [14] Z. Yin, H. Li, H. Li, L. Jiang, Y. Shi, Y. Sun, G. Lu, Q. Zhang, X. Chen, and H. Zhang, *ACS Nano* **6**, 74-80 (2012).
- [15] O. Lopez-Sanchez, D. Lembke, M. Kayci, A. Radenovic, and A. Kis, *Nature Nanotech.* **8**, 497-501 (2013).
- [16] H. Yuan, M. S. Bahramy, K. Morimoto, S. Wu, K. Nomura, B.-J. Yang, H. Shimotani, R. Suzuki, M. Toh, C. Kloc, X. Xu, R. Arita, N. Nagaosa, and Y. Iwasa, *Nature Phys.* **9**, 563-569 (2013).
- [17] H. Zeng, J. Dai, W. Yao, D. Xiao, and X. Cui, *Nature Nanotech.* **7**, 490-493 (2012).
- [18] K. F. Mak, K. He, J. Shan, and T. F. Heinz, *Nature Nanotech.* **7**, 494-498 (2012).
- [19] A. Splendiani. *et al.* *Nano Lett.* **10**, 1271-1275 (2010).
- [20] S. Das, H.-Y. Chen, A. V. Penumatcha, and J. Appenzeller, *Nano Lett.* **13**, 100-105 (2013).
- [21] I. Popov, G. Seifert, and D. Tománek, *Phys. Rev. Lett.* **108**, 156802 (2012).
- [22] J. Kang, W. Liu, D. Sarkar, D. Jena, and K. Banerjee, *Phys. Rev. X* **4**, 031005 (2014).
- [23] M. Amani, M. L. Chin, A. G. Birdwell, T. P. O'Regan, S. Najmaei, Z. Liu, P. M. Ajayan, J. Lou, and M. Dubey, *Appl. Phys. Lett.* **102**, 193107 (2013).
- [24] W. Liu, J. Kang, W. Cao, D. Sarkar, Y. Khatami, D. Jena, and K. Banerjee, *IEEE International Electron Devices Meeting*, 499-502 (2013).
- [25] H. Qiu, L. Pan, Z. Yao, J. Li, Y. Shi, and X. Wang, *Appl. Phys. Lett.* **100**, 123104 (2012).
- [26] W. Chen, E. J. G. Santos, W. Zhu, E. Kaxiras, and Z. Zhang, *Nano Lett.* **13**, 509-514

- (2013).
- [27] C. Gong, L. Colombo, R. M. Wallace, and K. Cho, *Nano Lett.* **14**, 1714-1720 (2014).
- [28] J. Kang, W. Liu, and K. Banerjee, *Appl. Phys. Lett.* **104**, 093106 (2014).
- [29] H. Jiang, *J. Phys. Chem. C* **116**, 7664-7671 (2012).
- [30] M. C. Toroker, D. K. Kanan, N. Alidoust, L. Y. Isseroff, P. Liao, and E. A. Carter, *Phys. Chem. Chem. Phys.* **13**, 16644 (2011).
- [31] L. Wirtz, A. Marini, and A. Rubio, *Phys. Rev. Lett.* **96**, 126104 (2006).
- [32] C.-H. Park, C. Spataru, and S. G. Louie, *Phys. Rev. Lett.* **96**, 126105 (2006).
- [33] L. Yang, C.-H. Park, Y.-W. Son, M.L. Cohen, and S. G. Louie, *Phys. Rev. Lett.* **99**, 186801 (2007).
- [34] L. Yang, J. Deslippe, C.-H. Park, M. L. Cohen, and S. G. Louie, *Phys. Rev. Lett.* **103**, 186802 (2009).
- [35] R. Fei, *et al.* *Phys. Status Solidi B* **8**, 1636–1643 (2013).
- [36] D. Y. Qiu, F. H. da Jornada, and S. G. Louie, *Phys. Rev. Lett.* **111**, 216805 (2013).
- [37] J. He, K. Hummer, and C. Franchini, *Phys. Rev. B* **89**, 075409 (2014).
- [38] R. Quhe. *et al.* *Sci. Rep.* DOI: 10.1038, **2**, 853 (2012).
- [39] J. B. Neaton, M. S. Hybertsen, and S. G. Louie, *Phys. Rev. Lett.* **97**, 216405 (2006).
- [40] A. H. Reshak and S. Auluck, *Phys. Rev. B* **68**, 125101 (2003).
- [41] G. Kresse and J. Furthmüller, *Comput. Mater. Sci.* **6**, 15-50 (1996).
- [42] G. Kresse and D. Joubert, *Phys. Rev. B* **59**, 1758-1775 (1999).
- [43] J. P. Perdew and Y. Wang, *Phys. Rev. B* **45**, 13244-13249 (1992).
- [44] F. Ortmann, F. Bechstedt, and W. G. Schmidt, *Phys. Rev. B* **73**, 205101 (2006).
- [45] H. J. Monkhorst and J. Pack, *Phys. Rev. B* **13**, 5188–5192 (1976).
- [46] P. A. Khomyakov, G. Giovannetti, P. C. Rusu, G. Brocks, J. van den Brink, and P. J. Kelly, *Phys. Rev. B* **79**, 195425 (2009).
- [47] Y. Ding, Y. Wang, J. Ni, L. Shi, S. Shi, and W. Tang, *Physica B* **406**, 2254-2260 (2011).
- [48] Y. Liang, S. Huang, R. Soklaski, and L. Yang, *Appl. Phys. Lett.* **103**, 042106 (2013).
- [49] R. Schlaf, O. Lang, C. Pettenkofer, and W. Jaegermann, *J. Appl. Phys.* **85**, 2732-2753 (1999).
- [50] Y. Li, C.-Y. Xu, B.-Y. Zhang, and L. Zhen, *Appl. Phys. Lett.* **103**, 033122 (2013).
- [51] S. Das, W. Zhang, M. Demarteau, A. Hoffmann, M. Dubey, and A. Roelofs, *Nano Lett.* **14**, 5733-5739 (2014).
- [52] J. Qiao, X. Kong, Z. X. Hu, F. Yang, and W. Ji, *Nat Commun* **5**, 4475 (2014).
- [53] V. Tran, R. Soklaski, Y. Liang, and L. Yang, *Phys. Rev. B* **89**, 235319 (2014).
- [54] Y. Y. Pan, H. X. Zhong, and J. Lu, in preparation (2015).
- [55] Y. J. Zhang, T. Oka, R. Suzuki, J. T. Ye, and Y. Iwasa, *Science* **344**, 725-728 (2014).

Table 1. Calculated interfacial properties of ML and BL MoS₂ on metal surfaces. The experimental cell parameters of the surface unit cells shown in Fig. 1 for various metals are under the metals. The corresponding lattice mismatches given. The equilibrium distance d_{S-M} is the averaged distance between the surface S atoms of MoS₂ and the relaxed positions of the topmost metal layer in the z direction. E_b is the binding energy per surface S atom between MoS₂ and a given surface. W_M and W are the calculated work functions for clean metal surface and metal surface adsorbed by MoS₂, respectively. Φ_v and Φ_L are the vertical and lateral SBH at the DFT level, respectively, of a MoS₂ transistor (see Fig. 7(b)); the SBH obtained in other DFT calculations, the GW-corrected SBHs, and the measured SBH are given below them in parenthesis for comparison. ΔE_f is the Fermi level shift of 2D MoS₂. The corresponding values for Sc and Ti surfaces in small mismatch are also given.

Metal	Mismatch	W_M (eV)	ML MoS ₂						BL MoS ₂					
			d_{S-M} (Å)	E_b (eV)	W (eV)	ΔE_f (eV)	Φ_v (eV)	Φ_L (eV)	d_{S-M} (Å)	E_b (eV)	W (eV)	ΔE_f (eV)	Φ_v (eV)	Φ_L (eV)
Sc	4.485%	3.593	1.786	1.181	4.369	-0.881	0.000	0.000	1.783	1.182	4.306	-0.944	0.000	0.000
3.308							(0.000) ^{GW}	(0.539) ^{GW}					(0.000) ^{GW}	(0.000) ^{GW}
(Å)	1.29%				4.192		0.000	0.000			4.300	-0.950	0.000	0.000
							(0.000) ^{GW}	(0.362) ^{GW}					(0.000) ^{GW}	(0.000) ^{GW}
Ti	6.791%	4.427	1.557	1.812	4.597	-0.653	0.000	0.187 ^b	1.560	1.848	4.616	-0.634	0.000	0.096
2.951							(0.000) ^a	(0.33) ^c					—	(0.065) ^d
(Å)							(0.000) ^{GW}	(0.731) ^{GW}					(0.000) ^{GW}	(0.276) ^{GW}
	2.99%				4.626		0.000	0.216			4.681		0.000	0.161
							(0.000) ^{GW}	(0.796) ^{GW}					(0.000) ^{GW}	(0.341) ^{GW}
Ag	5.367%	4.489	2.961	0.503	4.662	-0.588	0.000	0.252	2.917	0.547	4.763	-0.487	0.000	0.243
5.778(Å)							(0.000) ^{GW}	(0.832) ^{GW}					(0.000) ^{GW}	(0.423) ^{GW}
Ni	9.112%	5.222	2.094	0.830	5.001	-0.249	0.000	0.591	2.097	0.729	5.102	-0.148	0.000	0.582
4.984(Å)							(0.000) ^{GW}	(1.171) ^{GW}					(0.000) ^{GW}	(0.762) ^{GW}
Au	5.185%	5.226	3.405	0.307	5.173	-0.077	0.763	0.000	3.325	0.354	5.187	-0.063	0.667	0.000
5.768							(0.88) ^e	(0.000) ^e					—	—
(Å)							(1.343) ^{GW}	(0.000) ^{GW}					(0.833) ^{GW}	(0.000) ^{GW}
Pt	1.191%	5.755	2.476	0.570	5.444	0.194	0.000	0.546	2.438	0.634	5.476	0.226	0.000	0.504
5.549(Å)							(0.000) ^{GW}	(1.226) ^{GW}					(0.000) ^{GW}	(0.684) ^{GW}

^a DFT values from Refs. [21,28].

^b A significant SBH is observed in ML MoS₂-Ti junction at low drain-source voltage [23,24].

^c DFT value from Ref. [28].

^d Experimental value at a low temperature in Ref. [25].

^e DFT value from Ref. [27].

Table 2. The work functions W for metal surface adsorbed by MoS₂. The vertical Φ_v and lateral Φ_L SBH at the DFT level of a MoS₂ transistor (see Fig. 7(b)) when the lattice constants of metal surfaces are adjusted to that of MoS₂.

Metal	ML MoS ₂			BL MoS ₂		
	W (eV)	Φ_v (eV)	Φ_L (eV)	W (eV)	Φ_v (eV)	Φ_L (eV)
Sc	4.161	0.000	0.000	4.310	0.000	0.000
Ti	4.561	0.000	0.151	4.411	0.000	0.000
Ag	4.625	0.000	0.215	4.558	0.000	0.138
Ni	5.115	0.000	0.705	5.240	0.000	0.820
Au	5.058	0.000	0.813	5.211	0.000	0.559
Pt	5.432	0.000	0.648	5.079	0.000	0.659

Table 3. Tunneling barrier height ΔV , width w_B , and probabilities (T_B) through the ML (BL) MoS₂-metal interfaces.

Metal	ML MoS ₂			BL MoS ₂		
	ΔV (eV)	w_B (Å)	T_B (%)	ΔV (eV)	w_B (Å)	T_B (%)
Sc	0.000	0.000	100	0.000	0.000	100
Ti	0.000	0.000	100	0.000	0.000	100
Ag	3.003	0.916	19.68	2.911	0.904	20.61
Ni	0.785	0.327	74.33	0.822	0.336	73.20
Au	4.697	1.374	4.74	4.585	1.356	5.11
Pt	1.810	0.458	53.21	1.871	0.517	48.47

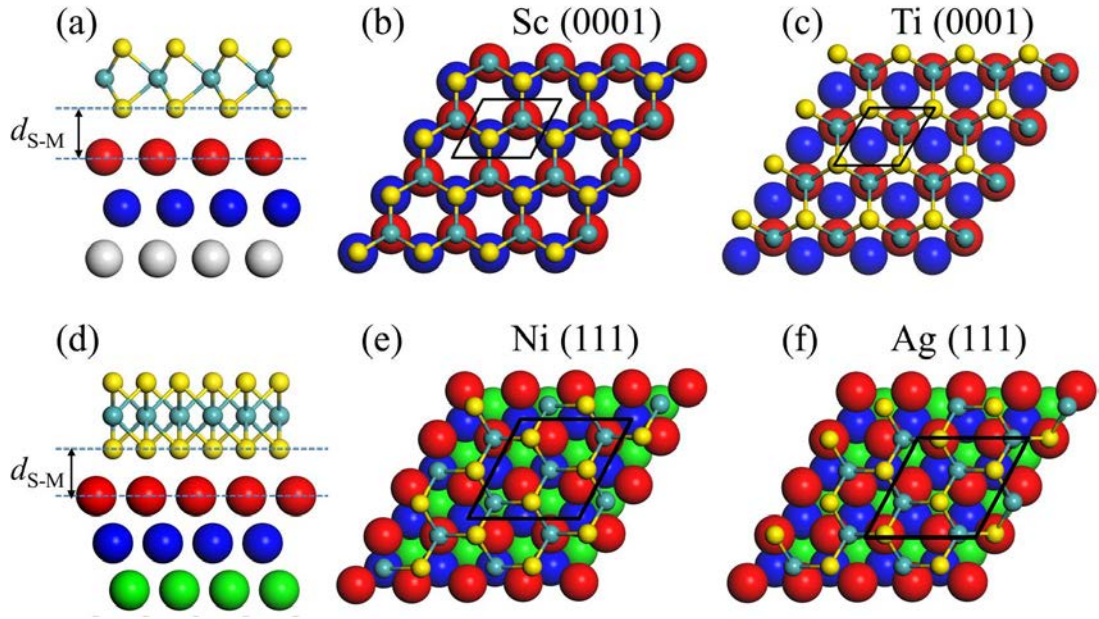


FIG. 1. Interfacial structures of the most stable configuration for ML MoS₂ on metal surfaces. (a) Side and (b) top views of ML MoS₂ on Sc(0001) surface. (c) Top view of MoS₂ on Ti(0001) surface. (d) Side and (e) top views of ML MoS₂ on Ni and Pt(111) surfaces. (f) Top view of MoS₂ on Ag and Au(111) surfaces. d_{S-M} is the equilibrium distance between the metal surface and the bottom layer MoS₂. The rhombi plotted in black line shows the unit cell for each structure.

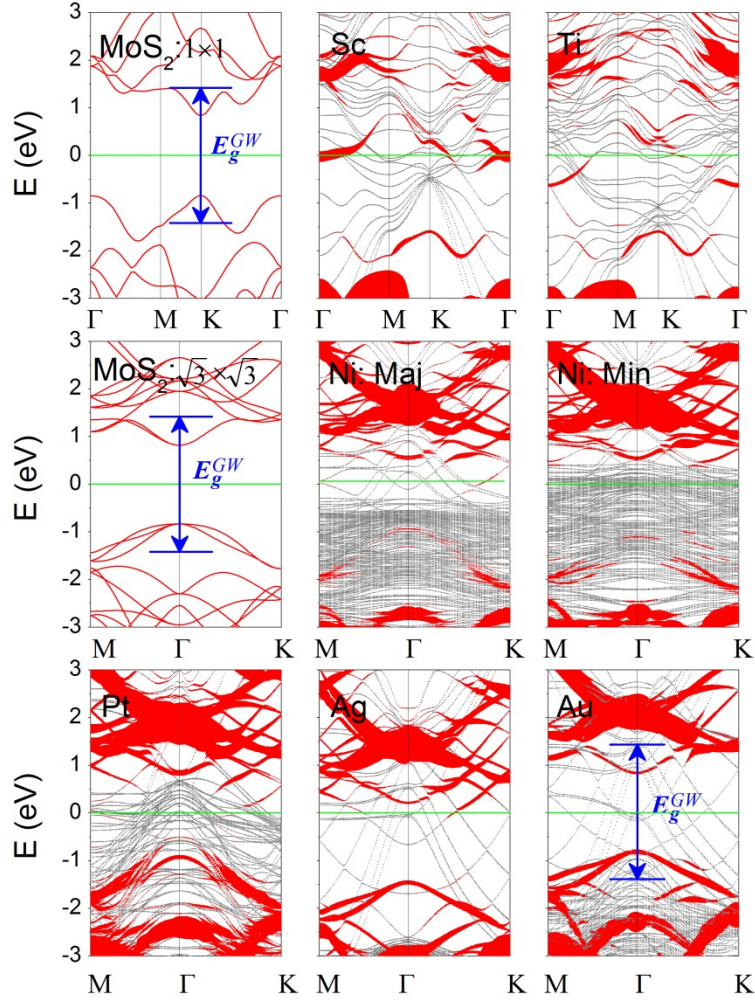


FIG. 2. Band structures of ML MoS₂ on Sc, Ti, Ni, Pt, Ag, and Au surfaces by the DFT method, respectively. The Fermi level is at zero energy. Gray line: metal surface bands; red line: bands of MoS₂. The line width is proportional to the weight. Blue line: the positions of CBM and VBM of MoS₂ after the GW-BGC correction. The labels Maj/Min indicate the majority-spin and minority-spin bands of MoS₂ on Ni surface. The band structure of free-standing ML MoS₂ calculated in a primitive unit cell and a $\sqrt{3} \times \sqrt{3}$ supercell are provided for comparison.

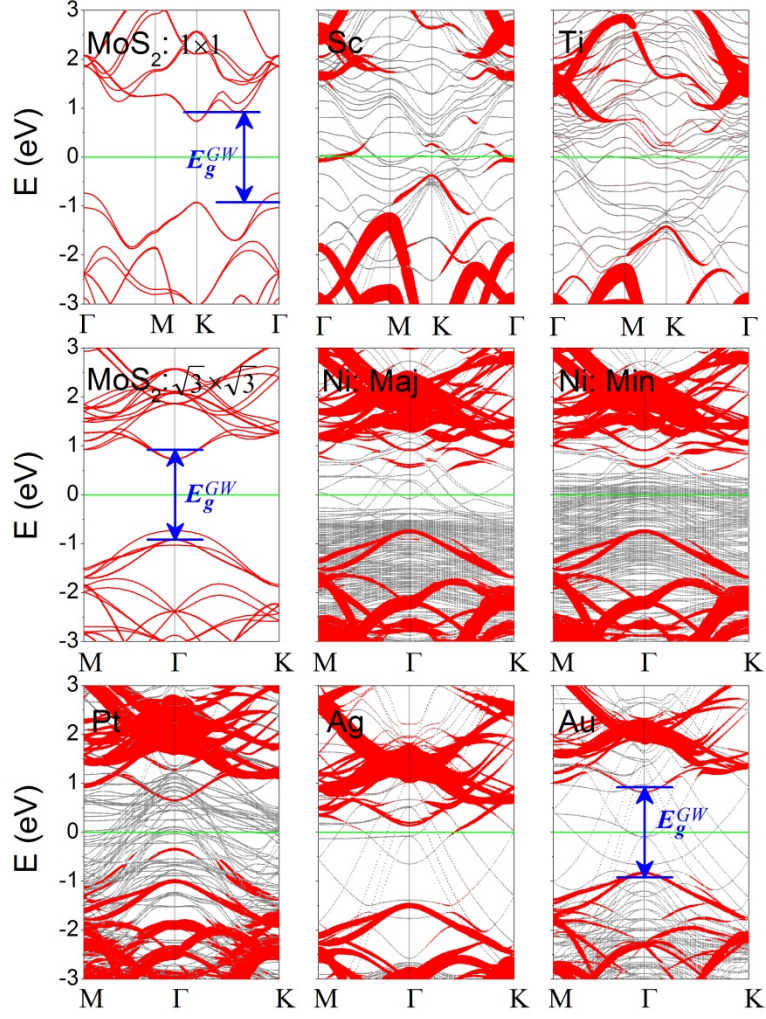


FIG. 3. Band structures of BL MoS₂ on Sc, Ti, Ni, Pt, Ag, and Au surfaces by the DFT method, respectively. The Fermi level is at zero energy. The gray (red) line denotes metal surface (BL MoS₂) bands. The line width is proportional to the weight. Blue line: the positions of CBM and VBM of MoS₂ at the GW-BGC scheme. The labels Maj/Min indicate the majority-spin and minority-spin bands of BL MoS₂ on Ni surface. The band structure of free-standing BL MoS₂ calculated in a primitive unit cell and a $\sqrt{3} \times \sqrt{3}$ supercell are provided for comparison.

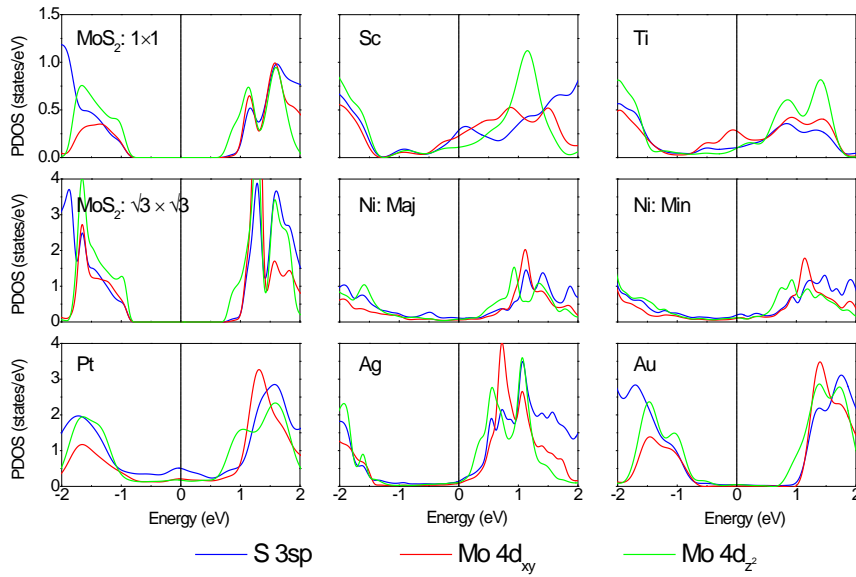


FIG. 4. Partial density of states (PDOS) (DOS on specified atoms and orbitals, for example, Mo-*d* (*d*-orbital on Mo)) of ML MoS₂ on Sc, Ti, Ni, Pt, Ag, and Au surfaces at the DFT level. The Fermi level is at zero energy. The PDOS of free-standing ML MoS₂ calculated in a primitive unit cell and a $\sqrt{3} \times \sqrt{3}$ supercell is provided for comparison.

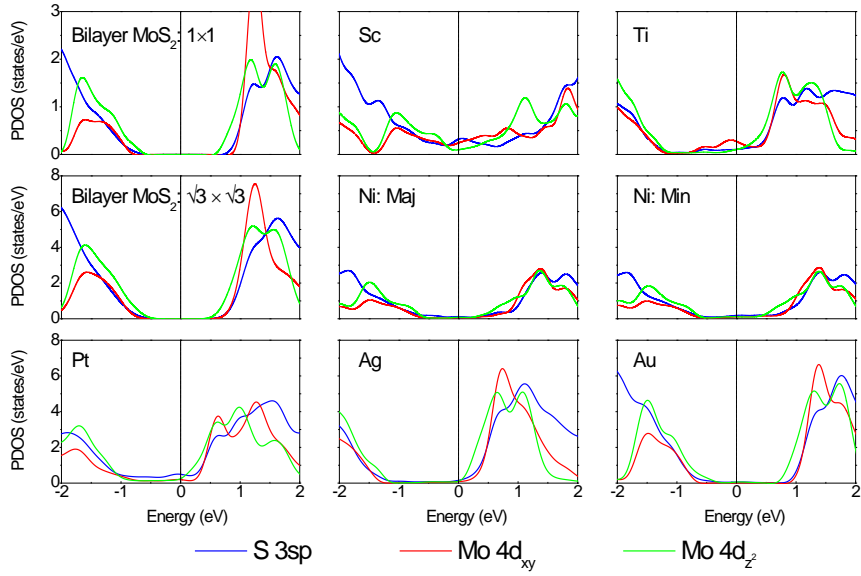


FIG. 5. PDOS of BL MoS₂ on Sc, Ti, Ni, Pt, Ag, and Au surfaces at the DFT level. The Fermi level is at zero energy. The PDOS of free-standing BL MoS₂ calculated in a primitive unit cell and a $\sqrt{3} \times \sqrt{3}$ supercell are provided for comparison.

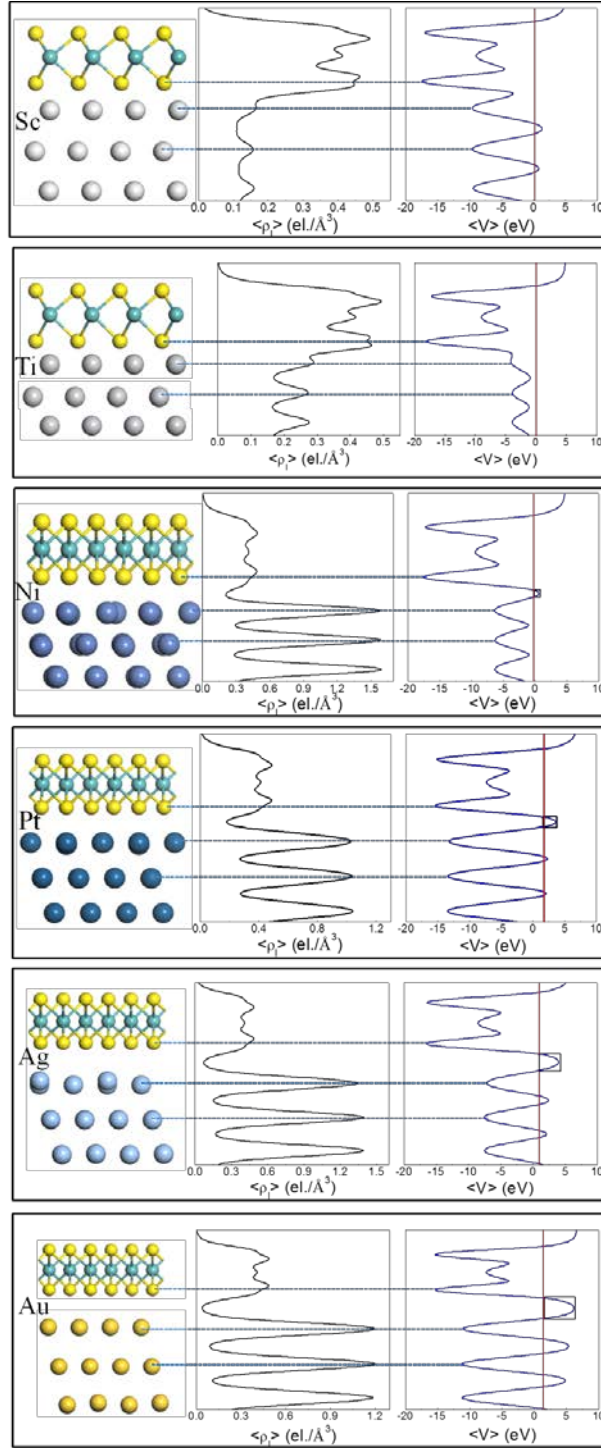


FIG. 6. Electronic structure at the interface between ML MoS_2 and metal at the DFT level. $\langle \rho_i \rangle$ is the average value in planes parallel to the interface of MoS_2 -metal. $\langle V \rangle$ is the average electrostatic potential in planes normal to the MoS_2 -metal interface. The dot lines indicate the location of the sulfur layer and the metal layers at the interface. The higher the ρ_i at the interface is, the higher the electron injection is.

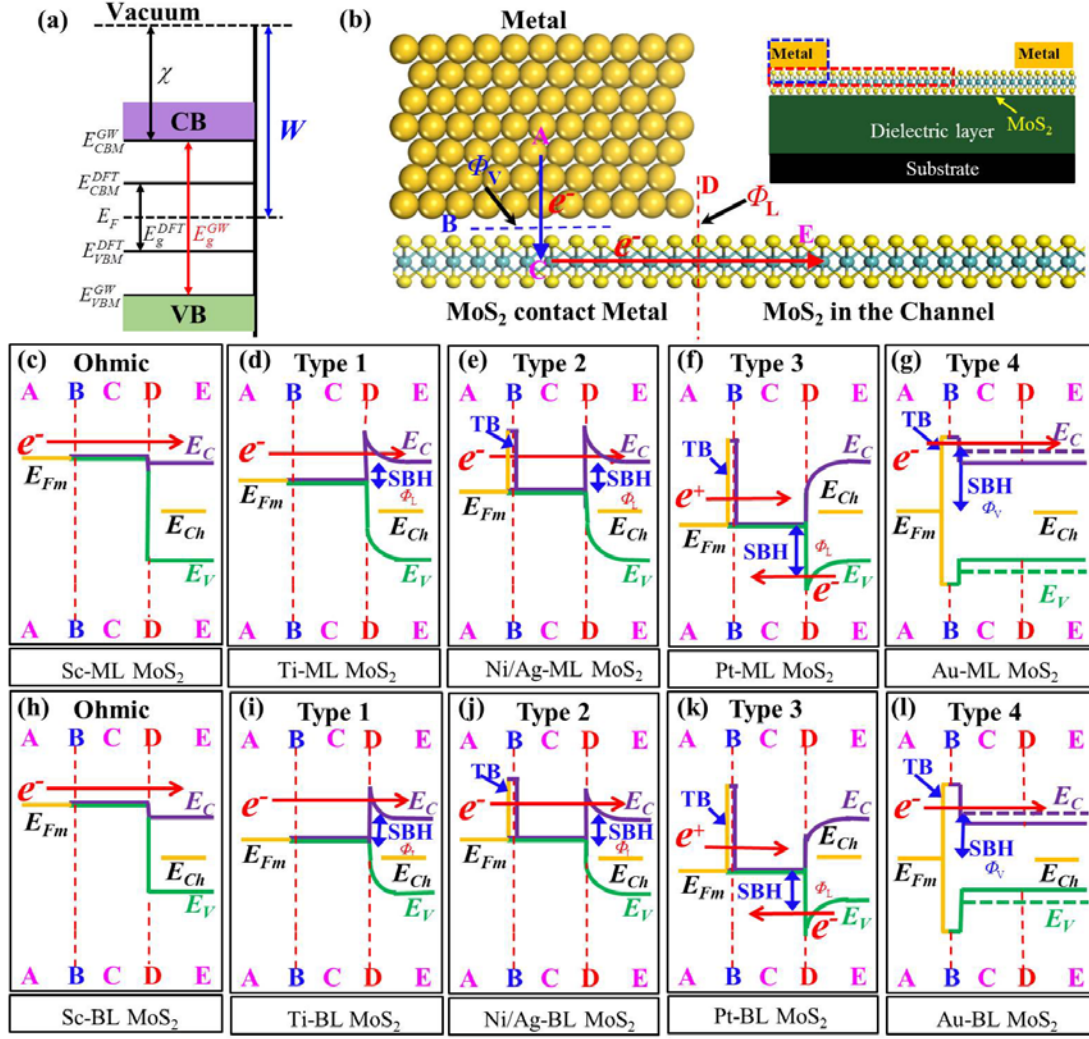


FIG. 7. (a) Schematic illustration of the absolute band positions with respect to the vacuum level at both DFT and GW levels. (b) Schematic cross-sectional view of a typical metal contact to 2D MoS₂. A, C, and E denote the three regions while B and D are the two interfaces separating them. Blue and red arrows show the pathway (A→B→C→D→E) of electron injection from contact metal (A) to the MoS₂ channel (E). Inset figure shows the typical topology of a MoS₂ field effect transistor (FET). (c)-(l) Eight band diagrams of (b) with at the DFT level, depending on the type of metals and MoS₂ layer number. The band edge positions with the GW correction are displayed in purple and green dashed line in panels (g) and (l). TB denotes transmission barrier. Examples (nature type) are provided at the bottom (top) of each diagram. E_{Fm} and E_{Ch} denote Fermi level of the absorbed system and channel MoS₂, respectively. Red arrows indicate the direction of electron flow.

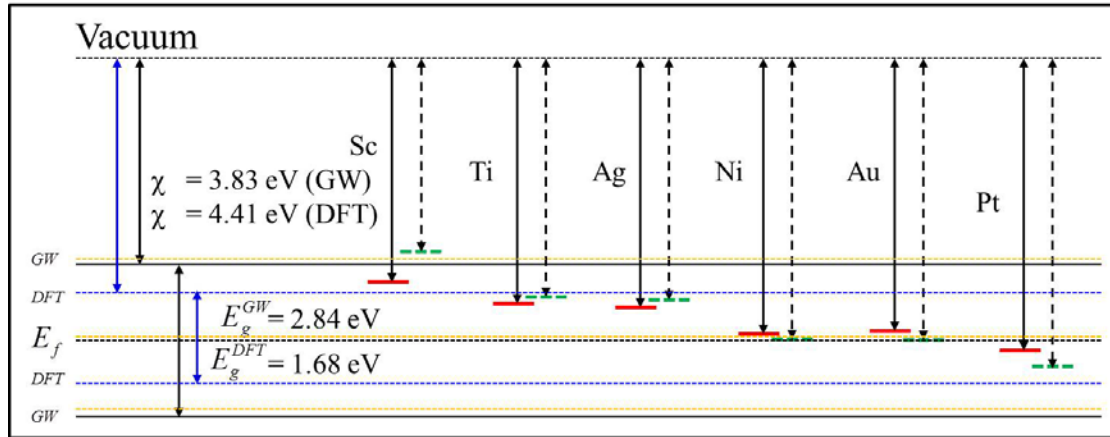


FIG. 8. Line-up of the metal Fermi level with the electronic bands of free -standing ML MoS₂ in terms of the calculated work function at the DFT level, with the Fermi level position of free-standing ML MoS₂ (blue dash lines) taken from the experiment [50]. The green dash line represents the Fermi level of pure metal, and the red solid line represents the Fermi level of the interfacial system. The absolute band positions calculated by the direct GW method [49] (yellow solid and dot lines) and the GW-BGC scheme (black dotted lines) are provided for comparison.

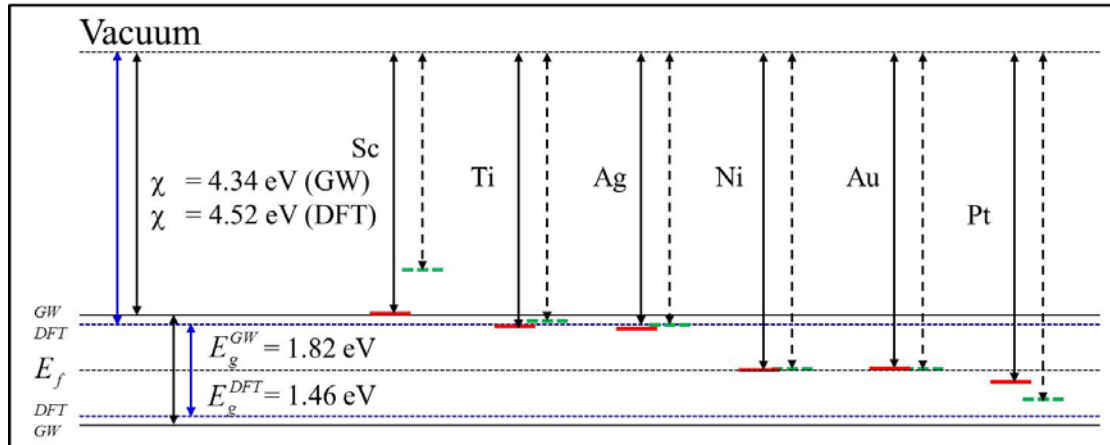


FIG. 9. Line-up of the metal Fermi level with the electronic bands of BL MoS₂ in terms of the calculated work function at the DFT level, with the Fermi level position of free-standing BL MoS₂ (blue dash lines) taken from the experiment [50]. The green dash (red solid) line denotes the Fermi level of pure metal (the interfacial system). The absolute band positions at the GW level (black dotted line) are provided for comparison.

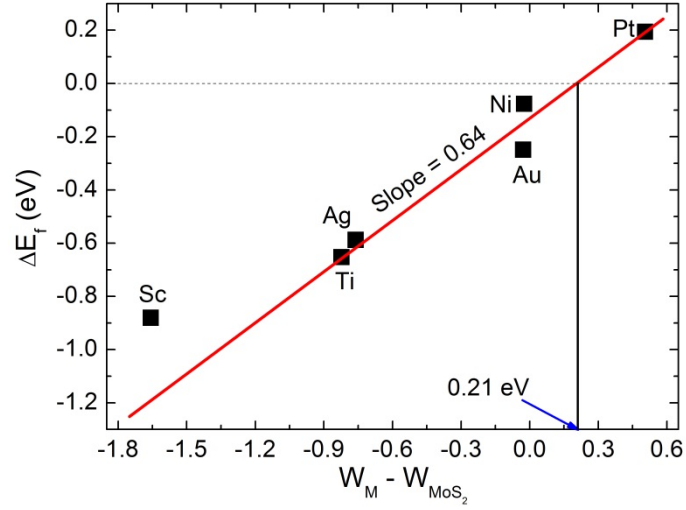


FIG. 10. Calculated Fermi level shift ΔE_f as a function of $W_M - W_{\text{MoS}_2}$, the difference between the clean metal and ML MoS_2 work functions at the DFT level. $W_M - W_{\text{MoS}_2} = 0.21$ eV is the cross point from *n*- to *p*-type doping. The red line is the fitting curve to the calculated points, and the slope of the line is 0.64.

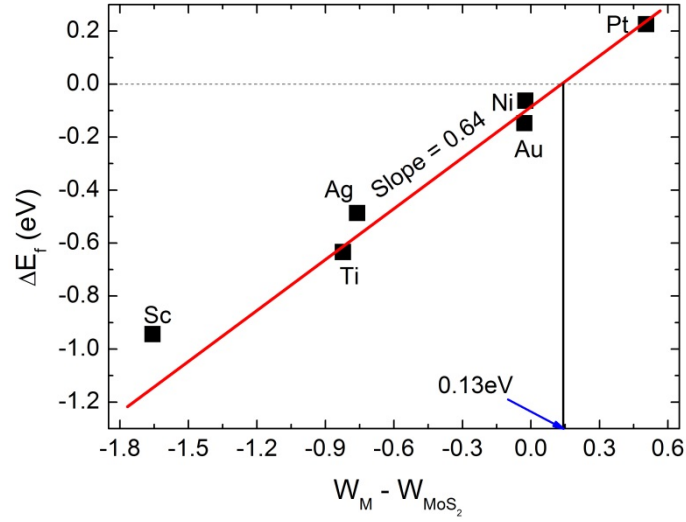


FIG. 11. Calculated Fermi level shift ΔE_f as a function of $W_M - W_{\text{MoS}_2}$, the difference between the clean metal and BL MoS₂ work functions at the DFT level. $W_M - W_{\text{MoS}_2} = 0.13$ eV is the cross point from *n*- to *p*-type doping. The red line is the fitting curve to the calculated points, and the slope of the line is 0.64.